Prussian blue as a co-catalyst for enhanced Cr(vi) photocatalytic reduction promoted by titania-based nanoparticles and aerogels

E. P. Ferreira-Neto, S. Ullah, A. P. Perissinotto, F. S. de Vicente, S. J. L. Ribeiro, M. A. Worsley, U. P. Rodrigues-Filho

December 20, 2022

New Journal of Chemistry

LLNL-JRNL-843437

Prussian blue as a co-catalyst for enhanced Cr (VI) photocatalytic reduction promoted by TiO_2 and SiO_2/TiO_2-based photocatalysts

Elias Paiva Ferreira-Neto[a,b*], Sajjad Ullah[b,c,d] Amanda Pasquoto Perissinotto[a], Fábio S. de Vicente[e], Sidney José Lima Ribeiro[b], Marcus Andre Worsley[f], Ubirajara Pereira Rodrigues-Filho[a*]

[a]Institute of Chemistry of São Carlos, University of São Paulo, 13560-970, São Carlos, SP, Brazil
[b]Institute of Chemistry, São Paulo State University (UNESP), 14800-060, Araraquara, SP, Brazil
[c]Institute of Physics, Federal University of Mato Grosso do Sul, 79070-900, Campo Grande, MS, Brazil
[d]Institute of Chemical Sciences, University of Peshawar, PO Box 25120, Peshawar, Pakistan
[e]Institute of Geosciences and Exact Sciences, Department of Physics, São Paulo State University (UNESP), 13500-970, Rio Claro, SP, Brazil
[f]Physical and Life Sciences Directorate, Lawrence Livermore National Laboratory, 94550, Livermore, CA, USA

*Corresponding authors: elias.p.ferreira@gmail.com (E. P. Ferreira-Neto), ubirajara@usp.br (U. P. Rodrigues-Filho)

Abstract

Hexavalent Chromium (Cr(VI)) is an obnoxious and highly toxic heavy metal that may present a serious threat to human health if present even in low concentrations in drinking water. Photocatalytic reduction of Cr(VI) to its less toxic Cr(III) state is a potential strategy to combat Cr(VI) pollution, but the efficiency of the process in low, especially in the absence of hole scavenger organic molecules. To address this problems and prepare efficient photocatalysts for Cr(VI) removal from water, in this study, we employed Prussian blue (PB) as a co-catalyst for improving the photoreduction performance of different high surface area (62–465 $m^2.g^{-1}$) TiO_2-based materials (TiO_2 nanoparticles and aerogels), silica-supported small anatase TiO_2 particles (SiO_2@TiO_2 core@shell), and silica-titania aerogels. The photocatalysts nanoparticles were surface-modified with different amounts (1.7–12.8% Fe) of nanocrystalline PB (crystallite size 6–9 nm) using photodeposition. The formation of PB was confirmed by XRD, SEM and Raman and FTIR spectroscopy. All the PB-modified photocatalysts exhibit better photocatalytic activity (65–100% reduction in 1h) as compared to unmodified photocatalysts (20–40% reduction) towards reduction of Cr (VI) in deionized water (non-acidic environment) and in the total absence of organic electron donors. The photocatalytic activity is dependent on the PB loading. Samples (PB2 series) with (3–3.7% Fe) exhibit the highest photoactivity (85–100%). It is especially important to note that the PB-modified photocatalysts exhibited this high photoactivity without any pH adjustment (non-acidic media) or addition of organic additives. To the best of our knowledge, this is the first report on the ability of PB to act as a co-catalyst in photocatalytic reduction reactions promoted by titania based catalysts. The simple approach reported herein can be followed to prepare new PB-photocatalyst systems with improved photocatalytic performance towards Cr (VI) reduction and other target applications.

1. Introduction

Pollution of fresh water bodies by a variety of toxic organic (dyes, pharmaceutical products, pesticides) and inorganic contaminants (heavy metals) is a serious environmental challenge of great concern that requires immediate attention. Water pollutants have not only affected aquatic life, but consumption of contaminated meat and produce has also been associated with numerous health ailments[1–3]. Among the heavy metals, hexavalent chromium (Cr(VI)) is an especially toxic and carcinogenic contaminant commonly present in wastewater from different industrial activities such as electroplating, pigment production, leather tanning, mining, metallurgy and others[4,5]. Owing to its high solubility and high mobility in water, Cr(VI) species are difficult to be removed from water bodies and present a serious threat to human health if present even in low concentrations in drinking water. On the other hand, Cr(III) species exhibit lower toxicity and can be easily removed by precipitation as $Cr(OH)_3$ using conventional water treatment techniques. Thus, treatment of Cr(VI) contaminants essentially involves reduction of Cr(VI) to Cr(III) species using different reductive removal methodologies such as bioremediation, electrocatalysis, chemical precipitation and photocatalysis [6].

Heterogeneous photocatalysis is regarded as a promising and sustainable approach for environmental remediation as it is (ideally) capable of promoting water purification by harnessing solar energy and employing only water and oxygen as reagents[7]. Upon photoexcitation with light of suitable energy, an electron is promoted from the valence band (VB) to conduction band (CB) of the photocatalysts, thus generating oxidative holes (in VB) and reductive electrons (in CV) which are capable of promoting the oxidative breakdown of organic pollutants and photocatalytic reduction reactions, respectively [8]. The photocatalytic reduction ability of photocatalysts can be usefully exploited for removal of heavy metals contaminants from water bodies [9]. In particular, several studies have reported the photocatalytic reduction of Cr(VI) using semiconductor catalysts as a promising approach for the treatment of chromate contaminated wastewater Despite the great potential of photocatalysis for the removal of heavy metal pollutant, particularly Cr(VI)) from water, the overall efficiency of such photocatalytic processes is still low and it is often necessary to add organic additives (as electron donors) and perform the reduction process in acidic media to achieve the desirable efficiency [6,10–12]. Doing so, however, offsets the advantages offered by photocatalytic process and raises concern over the feasibility of photocatalytic wastewater treatment. Thus, it is of great interest to develop new, cost-effective and more efficient photocatalytic systems that could be employed in wastewater treatment without requiring the addition of organic additives or acids during the photocatalytic reduction processes or other environmental applications.

Among the heterogeneous photocatalysts employed for environmental remediation applications, TiO_2–based nanomaterials are still the most widely studied photocatalysts due to their relatively higher photocatalytic efficiency and other desirable characteristics including good (photo)chemical stability, low-cost and ease of preparation, among others [13,14]. Nevertheless, a number of drawbacks associated with the use of TiO_2 limit its performance as a photocatalyst. These limitations of TiO_2 may be related to its physical properties (nanoparticle agglomeration and uncontrolled crystallite growth and phase transformation upon during thermal treatments) [15–17] or its intrinsic electronic properties (lack of visible light photoactivity, high rate of electron-hole recombination) [18,19]. Both of these characteristics of TiO_2 diminish the quantum yield of the photocatalytic process and lower the probability of multi-electron redox reactions (including Cr(VI) reduction) to occur. Formation of nanocomposite materials by modification of TiO_2 with metal nanoparticles, metallic complexes, or other semiconductor nanomaterials is an important and interesting strategy to yield electronic coupled photocatalysts with improved performance in relation to overall photocatalytic activity, stability and visible light absorption capacity [20,21].

Ferric hexacyanoferrate ($Fe_4[Fe(CN_6)]_3$), commonly known as Prussian Blue (PB), is one of the oldest synthetic metal coordination compounds and the main member of an archetypical class of cyanometallates solid-state frameworks (Prussian Blue Analogues) [22,23]. Prussian Blue is a mixed-valence compound in which the simultaneous occurrence of both nitrogen-coordinated high-spin Fe(III) sites and carbon-coordinated Fe(II) low-spin sites results in unique electronic, catalytic and magnetic properties [22–26]. TiO_2-Prussian Blue nanocomposites prepared by chemical, photochemical and electrochemical methods were previously reported by different authors [27–29], the obtained materials being mostly explored for electrochemical applications but also as photoactive materials [30–34]. The photoactive behavior of such systems is based on the photo-induced electron transfer from the semiconductor titania particle towards the deposited PB layer. Upon UV excitation, electrons photoexcited to the titania conduction band have enough redox potential to reduce PB into its reduced form Prussian White (PW). Reduction of high-spin Fe(III) sites lead to color bleaching and change in magnetic susceptibility of PB layer, thus yielding photochromic and photomagnetic properties. Additionally, *in-situ* generated PW species may catalytically reduce adsorbed species such as metal ions and organic molecules, as demonstrated by electroanalytical studies employing PB-modified electrodes [35,36].

Based on such previous reports, in this study we propose its use as a co-catalyst for the enhanced Cr (VI) photocatalytic reduction promoted by TiO_2 and SiO_2/TiO_2-based photocatalysts. Even though TiO_2-PB was previously explored in photoactive based applications (photovoltaic, photochromic and photomagnetic materials), the photocatalytic activity of TiO_2-PB system has remained understudied. To the best of our knowledge, there is only one report on the use of TiO_2-PB as heterogeneous photo-Fenton catalyst [32] and no studies detailing the intrinsic photocatalytic activity of the material towards water contaminants. Different TiO_2-based materials were used in this study: (i) conventional TiO_2 nanoparticles, (ii) silica-supported small anatase TiO_2 (SiO_2@TiO_2 core@shell) particles, (iii) TiO_2 aerogel particles and (iv) two different silica-titania aerogels (SiO_2@TiO_2 core@shell aerogels and SiO_2-TiO_2 mixed aerogels). Thus the main objective of the present study is to explore the role of PB as a co-catalyst in improving the photoreduction performance of the different TiO_2-based materials mentioned above and to find the best photocatalytic system for Cr(VI) removal from water under practically feasible conditions.

2. Experimental

2.1. Reagents

Titanium (IV) dioxide anatase nanoparticles (TiO_2-A, 99.9%, Sigma-Aldrich), titanium (IV) tetrachloride ($TiCl_4$, 99%, Sigma-Aldrich), titanium (IV) isopropoxide (TiP, 97%, Sigma-Aldrich), tetraethylortosilicate (TEOS, 98% Sigma-Aldrich), potassium hexacyanoferrate(III) ($K_3Fe(CN)_6$, 99%, Sigma-Aldrich), iron (III) nitrate nonahydrate ($Fe(NO_3)_3.9H_2O$, 99%, Sigma-Aldrich), potassium dichromate ($K_2Cr_2O_7$, 99%, Synth), 1,5-diphenyl carbazide (DPC, 99% VETEC), propylene oxide (PO, 99% Sigma-Aldrich), ammonium hydroxide (NH_4OH, 28%, Sigma-Aldrich), potassium bromide (KBr, spectroscopic grade, Sigma-Aldrich), N,N-dimethylformamide (DMF, anhydrous, Sigma-Aldrich), isopropanol (HPCL grade, Panreac), absolute ethanol (HPCL grade, Panreac), hydrochloric acid (HCl, 37%, QHEMIS), nitric acid (HNO_3, 35%, QHEMIS) and sulfuric acid (H_2SO4, 98%, QHEMIS) were purchased from respective suppliers and used without further purification.

2.2. Preparation of SiO_2-TiO_2 particles and aerogels photocatalysts

Silica-titania particles and aerogel photocatalysts were prepared based on sol-gel methodologies earlier developed and published by our group [37,38]. The SiO_2@TiO_2 core@shell particles (denoted as ST, henceforth) were synthesized by deposition of TiO_2 on Stober silica (SiO_2) spheres by solvent-controlled hydrolysis of TiP alkoxide precursor. The method involves pre-adsorption of TiP on SiO_2 sphere from a mixed alcohol solvent (1:3 isopropanol: ethanol) followed by dropwise addition of water-solvent mixture to complete the hydrolysis of TiP and allow condensation of the hydrolyzed products on the surface of SiO_2 particles. The amorphous titania in these ST samples was crystallized using hydrothermal treatment (110 °C, 24h) in a homemade Teflon-lined brass hydrothermal reactor. The ST samples were dried at 60 °C for 24h and annealed at 600 °C for 1h (heating rate = 15 °C/min) to further increase titania crystallinity. Further details can be found in our earlier studies [37,39].

A $TiCl_4$–based sol-gel route was used to prepare nanostructured SiO_2@TiO_2 core@shell aerogels (denoted as ST-TID) and SiO_2-TiO_2 mixed silica-titania aerogels (denoted as ST-EAG), employing a $TiCl_4$/DMF solution as precursor solution. The ST-TID were prepared by thermo-induced deposition (TID) method. To prepare ST-TID aerogels, SiO_2 wet gels were soaked $TiCl_4$/DMF precursor solutions containing trace amount of H_2O for 24 h and subsequently heated at 80 °C for 24 h in an oven to achieve thermolytic deposition of TiO_2 on SiO_2 and thus obtain ST-TID wet-gels. The ST-EAG gels were prepared by epoxide-assisted gelation (EAG) method using the same $TiCl_4$/DMF precursor solutions and propylene oxide as gelification agent and pre-prepared SiO_2 aerogel powder as the silica source [38]. The SiO_2 aerogel powder was mixed with $TiCl_4$/DMF solution and, after 24 h of stirring, gelation was induced by the addition of a DMF/propylene oxide mixture to obtained ST-EAG wet-gels. TiO_2 wet gel (TiO_2-EAG) were prepared by a similar procedure without addition of SiO_2 aerogel particles. After their preparation, obtained wet gels (ST-TID, ST-EAG and TiO_2-EAG) were aged for 24 h at room temperature, washed once with DMF and several times with ethanol and acetone before being converted into dry aerogels by CO_2 supercritical drying (P= 1500 psi, T= 50 °C). The obtained aerogel monoliths were ground into fine powders and calcined at 600 °C. The details of synthesis of aerogel samples have been reported elsewhere [38].

2.3. Photocatalysts modification with Prussian Blue (PB)

A photo-assisted deposition method [29] was used to deposit PB (ferric hexacyanoferrate, $Fe_4[Fe(CN_6)]_3$) on the surface of different photocatalysts (TiO_2-A, TiO_2-EAG, ST, ST-TID and ST-EAG) particles or aerogels. For this purpose, 125 mg of the photocatalyst powder were dispersed in 100 mL of an aqueous suspension of $K_3[Fe(CN)_6]$ by sonication and the mixture was kept under magnetic stirring for 4 h. The mixture was then transferred to double-jacket borosilicate reactor (maintained at 22 °C through water circulating in the outer part) and 50 mL acidified $Fe(NO_3)_3$ solution (prepared in 0.1 $mol.L^{-1}$ HNO_3) was drop-wise added to the reactor while being continuously illuminated with UV light from a 150W Xe/Hg lamp (LightningCure, Hamamatsu, Japan) placed a distance of 9 cm from the reactor (Fig. 1b). After 1h of continuous irradiation and the resulting blue color suspension was centrifuged to separate PB-modified photocatalysts particles. The precipitates thus obtained were washed once with dilute (0.1 $mol.L^{-1}$) HNO_3 and twice with deionized water and then dried in an oven at 70 °C. The molar concentrations of $K_3[Fe(CN)_6]$ and $Fe(NO_3)_3$ were varied to deposit different amounts of PB on the surface of photocatalysts (Table 1).

2.4. Characterization techniques

X-ray diffractograms (2θ range = 10–80, step = 0.020°) of the samples were obtained using a D8 Advance diffractometer (Bruker, Germany), operated at 40 mA and 40 V and employing Ni-filtered Cu Kα X-ray (0.154 nm) radiation. FTIR spectra (4000–400 cm^{-1}, resolution 4 cm^{-1}) of the samples (3 mg sample + 100 mg KBr) pressed into pellets were collected using an IRAffinity-1S spectrophotometer (Shimadzu, Japan). Raman spectra were obtained using a Nicolet Almega Confocal Raman spectrometer coupled to an Olympus microscope (Thermo Fisher Scientific, USA). The spectra were collected using HeNe laser (λ = 632.8 nm) operated at 13% intensity as a source of excitation, accumulating 16 scans with a 10 s collection time. Scanning electron microscopy (FEG-SEM) images of the samples deposited on monocrystalline silicon substrates and sputter-coated with a thin (~ 6 nm) gold layer were obtained using an Inspect F-50 (FEI, Netherland) microscope, equipped with an Everhart–Thornley SE detector and a field emission gun (FEG) and operating at 5 kV electron beam accelerating voltage. Samples for transmission electron microscopy (TEM) analysis were deposited from a dilute suspension onto copper-coated copper minigrids (CFC-200Cu, EMS, USA) and analyzed using a Philips CM-200 Super Twin (FEI,, USA) microscope operating at a maximum acceleration voltage of 200 kV. X-Ray Fluorescence (XRF) spectroscopy was employed for a semi-quantitative elemental analysis of the sample using the standardless analysis package Omnian (PANalytical, Netherlands). The XRF measurements (acquisition time 840 s) were performed on benchmark MiniPal4 (PANalytical, Netherlands) energy-dispersive spectrometer equipped with a rhodium tube as X-ray source. Nitrogen (N_2) physisorption measurements were performed on an ASAP 2010 Micromeritics equipment (Micromeritics, USA). These samples were heated at 120 °C for 12 hours to remove adsorbed water. Specific surface area (S_{BET}) was determined from the adsorption/desorption isotherms using the Brunauer–Emmett–Teller (BET) method, total pore volume (V_p), as the volume of nitrogen adsorbed at a point close to the nitrogen saturation pressure and average pore size (l_p) as $l_p = 4V_p/S_{BET}$. Pore size distribution (PSD) analysis was carried out using DFT Plus Micromeritics software based on the classical Kelvin equation and the Harkins and Jura isotherm model for cylindrical pores [40,41].

2.5. Photocatalytic reduction of hexavalent chromium (Cr(VI))

The photo-reduction reaction of Cr(VI) was used to evaluate the photo-reducing capacity of the photocatalysts before and after modification with PB. For this purpose, 35 mg of the photocatalyst was dispersed in 35 mL water by sonication and then mixed with 35 mL of $K_2Cr_2O_7$ solution (containing 20 mg.L^{-1} of Cr (VI)). The photocatalysts/ $K_2Cr_2O_7$ mixture was allowed to stir in dark for 30 min and then illuminated with UV light from the Xe/Hg lamp mentioned earlier. Sample aliquots were withdrawn at 10 min interval, centrifuged (to separate the photocatalyst particle) and the concentration of Cr(VI) in the supernatant layer was monitored spectrophotometrically. For this purpose, Cr(VI) was first converted to a colored specie (λ_{max}= 540 nm) employing 1,5 diphenylcarbazide, DPC) as a complexing agent [42]. For this purpose, 200 µL of the sample (supernatant part) were added to a solution containing H_2O (1 mL), 1,5 diphenylcarbazide solution (0.2 mL of 0.5 g/L solution in acetone) and H_2SO_4 (0.1 mL) which led to the immediate formation of a pinkish solution the intensity of which depends on the amount of Cr(VI) present in the sample. The absorbance of this complex at 540 nm was monitored using a UV-visible spectrophotometer.

3.1 Results and Discussion

3.1. Modification of photocatalysts with Prussian blue (PB) co-catalyst

The photocatalysts nanoparticles (TiO_2-A, ST) and aerogels (TiO_2-EAG, ST-TID, ST-EAG) were surface-modified with PB using the photodeposition methodology developed by Tada and co-workers [29]. This method employs $[Fe(CN)_6]^{-3}$ and an Fe^{3+} salt as molecular precursors and is based on the fact that photo-excited electrons in the conduction band (CB) of TiO_2 are capable of reducing $[Fe(CN)_6]^{-3}$ in solution which, in the presence of Fe^{3+} cations, triggers PB nucleation/growth selectively on the surface TiO_2 particles. Fig. 1a illustrates the process and reactions involved in PB photodeposition on TiO_2-based materials. During PB photodeposition on the surface of photocatalyst samples, we observed a noticeable color change of the reaction mixture from yellow (color of $[Fe(CN)_6]^{-3}$ precursor) to green and finally to intense blue (Fig. 1b), indicating successful deposition of PB on these materials. The formation of PB was confirmed by vibrational spectroscopy and its % loading was determined by XRF analysis.

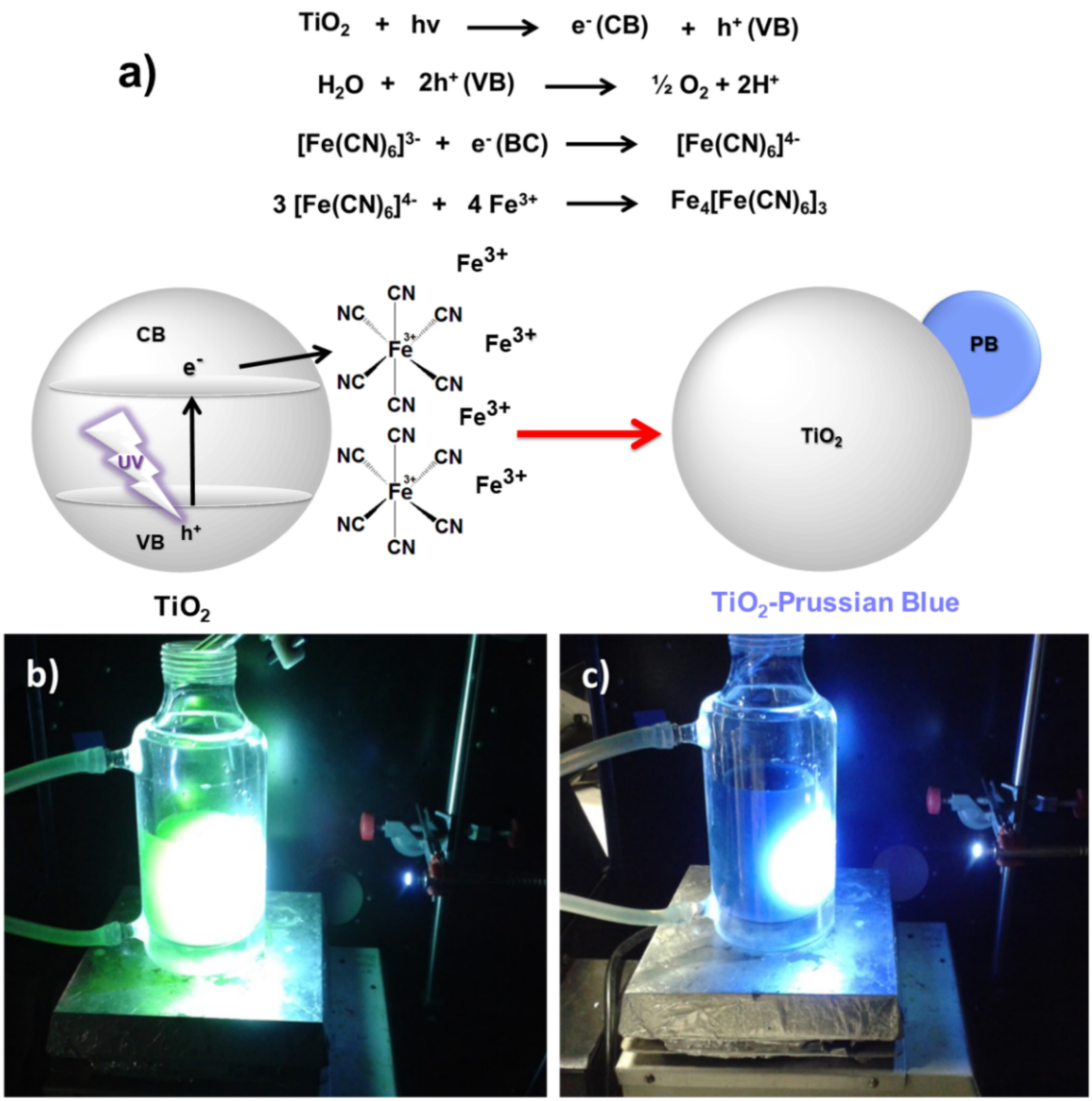

Figure 1. (a) Illustrative scheme and reactions involved in Prussian blue photodeposition process the surface of titania-based photocatalysts. Digital photographs showing PB photodeposition on $SiO_2@TiO_2$ particles as noticed from a color change from (b) light yellow (before illumination) to (c) intense blue (after illumination for 1h)

3.1.1 X-ray Fluorescence analysis (% TiO_2 and Fe loading)

As mentioned earlier, the amounts of iron-based precursors ($K_3[Fe(CN)_6]$ and $Fe(NO_3)_3$) were varied to photodeposit different amounts of PB on the surface of photocatalysts (Table 1). Resultantly, a notable change in coloration was observed in these different samples, with the final blue color progressively becoming more intense with the increase in PB precursors' concentration (inset Fig. 2). XRF analysis was thus employed to quantify the PB (%Fe) and TiO_2 contents of each sample (Table 1). Importantly, an almost linear correlation between %Fe loading (determined by XRF) of the samples (ST-PB series) and the total molar amount of Fe-based precursors added in the photodeposition (Figure 2) confirms the effectiveness of the photodeposition process and that the PB loading of the samples can be easily tuned by simply changing the precursors concentration. Moreover, it is worth noting that %Fe loading of different TiO_2-materials used in this work is very similar (3–3.7%) for a given irradiation time (1h) and precursors concentration, indicating that the amount photodeposited PB does not vary significantly with type or chemical composition of titania or silica-titania based photocatalysts even though they show quite different textural and photocatalytic properties [37,38].

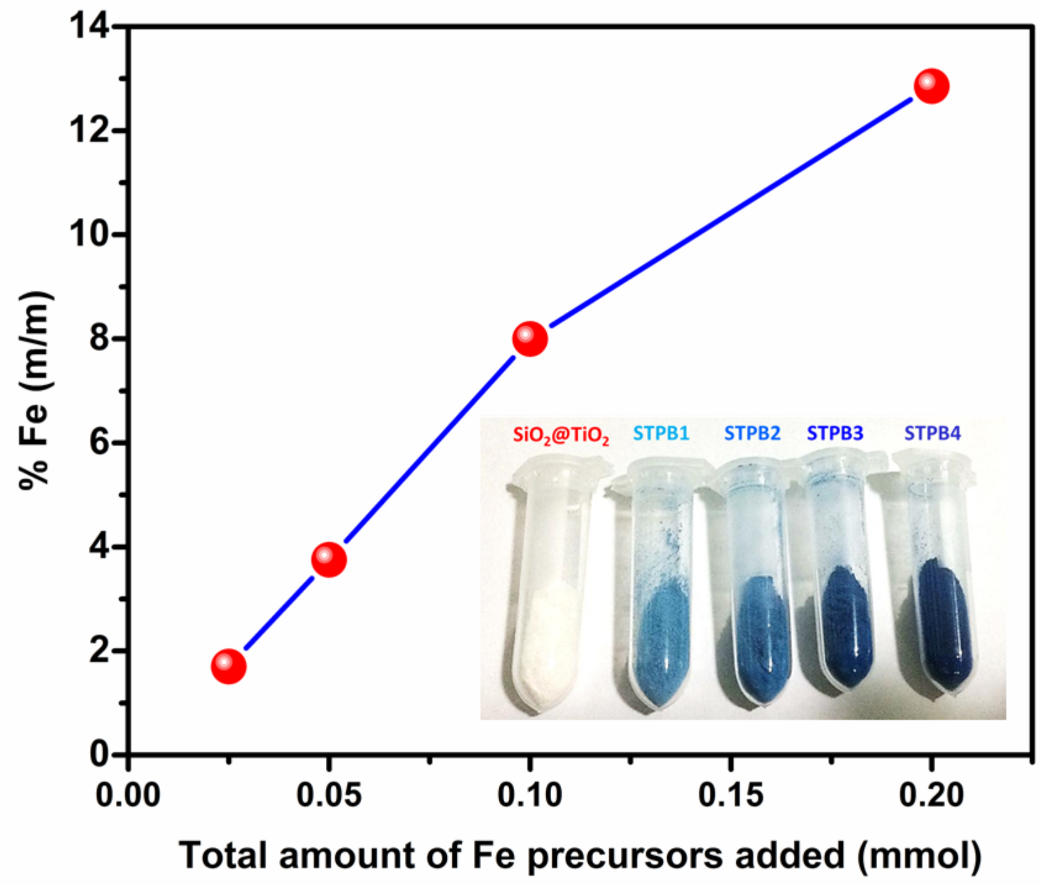

Figure 2. Variation of %Fe determined by XRF analysis for $SiO_2@TiO_2$-PB samples (ST-PB series) as function of initial amount of iron-based precursors added during photodeposition process (total amount of Fe added in mmol). The inset shows digitals photographs of the corresponding samples.

Table 1. Summary of the prepared PB-modified TiO_2 and SiO_2-TiO_2 samples, showing their respective initial composition (%TiO_2 determined by XRF), amounts of iron-based precursors employed during photodeposition process and Fe loading (mass %) values determined by XRF analysis.

Sample	**Base photocatalyst**	**Initial TiO_2 loading**	**$K_3[Fe(CN)_6]$ mmol**	**$Fe(NO_3)_3$ mmol**	**%Fe**
ST-PB1	SiO_2@TiO_2 particles	21%	0.0125	0.0125	1.7%
ST-PB2	SiO_2@TiO_2 particles	21%	0.025	0.025	3.7%
ST-PB3	SiO_2@TiO_2 particles	21%	0.05	0.05	8.0 %
ST-PB4	SiO_2@TiO_2 particles	21%	0.1	0.1	12.8%
ST-EAG-PB2	EAG SiO_2/TiO_2 Aerogel	60%	0.025	0.025	3.0%
ST-EAG-PB3	EAG SiO_2/TiO_2 Aerogel	60%	0.05	0.05	6.9%
ST-TID-PB2	TID SiO_2@TiO_2 Aerogel	65%	0.025	0.025	3.6%
ST-TID-PB3	TID SiO_2@TiO_2 Aerogel	65%	0.05	0.05	6.2%
TiO_2-EAG-PB2	EAG TiO_2 Aerogel	100%	0.025	0.025	3.7%
TiO_2-EAG-PB3	EAG TiO_2 Aerogel	100%	0.05	0.05	7.9%
TiO_2-A-PB2	TiO_2 NPs Sigma-Aldrich	100%	0.025	0.025	3.2%
TiO_2-A-PB3	TiO_2 NPs Sigma-Aldrich	100%	0.05	0.05	6.0%

3.1.3 Molecular Vibrational spectroscopy study (FTIR and Raman)

The formation of PB on the surface of the photocatalysts was confirmed by FTIR and Raman spectroscopy. Based on assignment of the vibrational modes of PB analogues by Kettle et al [43], PB is expected to show three cyanide (C≡N) stretching vibrational modes, two of which are Raman-active (A_{1g} and E_g modes) and one infrared-active (T_{1u} mode). The FTIR spectrum of representative ST-PB sample indicates the presence of vibrational modes characteristics of SiO_2-TiO_2 composites [44], as identified in Fig.3a. The broad band around 3400 cm^{-1} (O–H stretching) may come from adsorbed water molecule or surface hydroxyl groups of SiO_2/TiO_2 material. Of greater relevance is the signature FTIR band of PB at around 2081 cm^{-1} which originates from the stretching of C≡N bonds (T_{1u} vibrational mode) present in cyanometallate extended network of PB. As expected, the intensity of this characteristic vibrational band of PB increases with the increase in the PB content of the samples (inset, Fig. 3a).

The characteristic FTIR vibrational modes of cyanide ligands (normally occurring at 2040 cm^{-1} for isolated ferrocyanide ions) are quite sensitive towards coordination to metal centers and often shift to higher wavenumbers upon coordination of the ferrocyanide nitrogen terminations to metallic centers (as in Fe(II)–C–N–M) [24]. Since the FTIR spectra of our PB-modified samples show the cyanide vibrational modes at high wavenumbers (2083–2077 cm^{-1}) (Figs. 3a.b), it confirms the formation of PB extended network formed by Fe(II)–C–N–Fe(III) bridging bonds. Moreover, the FTIR band positions observed in our samples are also consistent with the values reported for pure PB (2070 cm^{-1}) and TiO_2-PB composite (2088 cm^{-1}) [29,45]. The same vibrational mode (C≡N linkages) is Raman active and gives rise to a strong Raman band around 2150 cm^{-1} (totally symmetrical A_{1g} mode) with a shoulder around 2090 cm^{-1} (E_g mode) [24,43] in the Raman spectra of our SiO_2-TiO_2-PB materials (Fig. 3c) which further confirms the formation of PB in these samples.

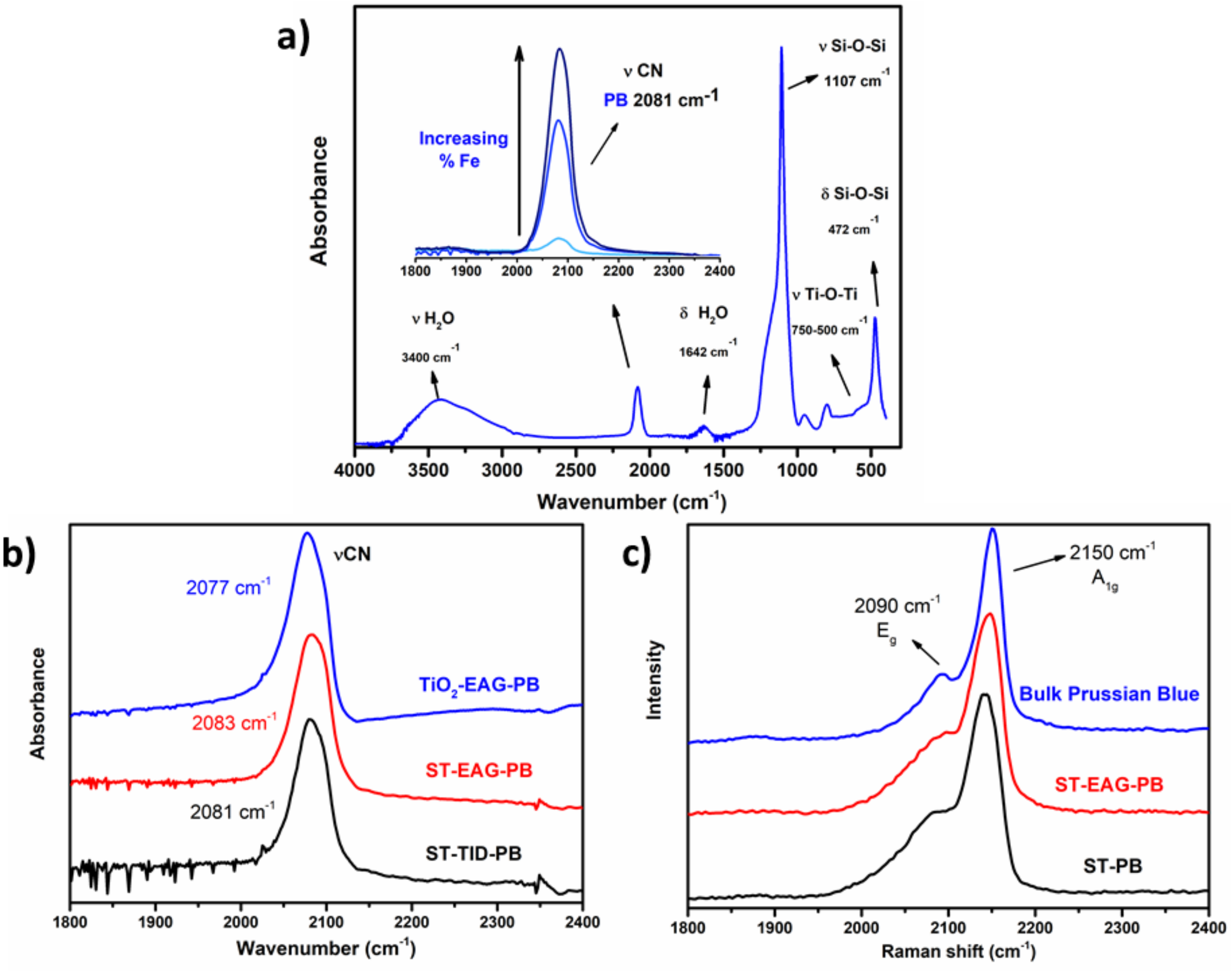

Figure 3. a) FTIR spectra of ST-PB sample. The inset shows the increase in intensity of C≡N stretching band as function of PB content of the samples. (b) The C≡N stretching virbation region for PB-modified titania and silica-titania aerogels (ST-TID-PB and ST-EAG-PB). (c) Raman spectra of PB-modified photocatalysts particles (ST-PB) and aerogels (ST-EAG-PB) as compred to the spectrum of pure bulk PB sample.

3.1.4 X-ray diffraction analysis

The formation of PB in different samples and its crystalline structure was studied using XRD analysis (Figure S1 and Figure 4). All samples exhibit the characteristic diffraction peaks of anatase except the pure TiO_2 aerogels which show additional diffraction peaks of rutile phase (Figs. 4a,b). The broader feature centered around 22° corresponds to amorphous SiO_2 in these silica-titania samples. In addition to the characteristic diffraction peaks of TiO_2, additional diffraction peaks (marked with *) are observed in diffractograms of all samples except STPB-1 (which has the lowest Fe concentration, see Figure S1) at 2θ values of 17.8°, 35.4° and 39.8°, which are attributed to the (200), (400) and (420) planes of the fcc crystalline structure of PB [46]. The absence of these characteristic diffraction peaks of PB in ST-PB1 samples may be related to PB loading below the limit of detection for the technique.

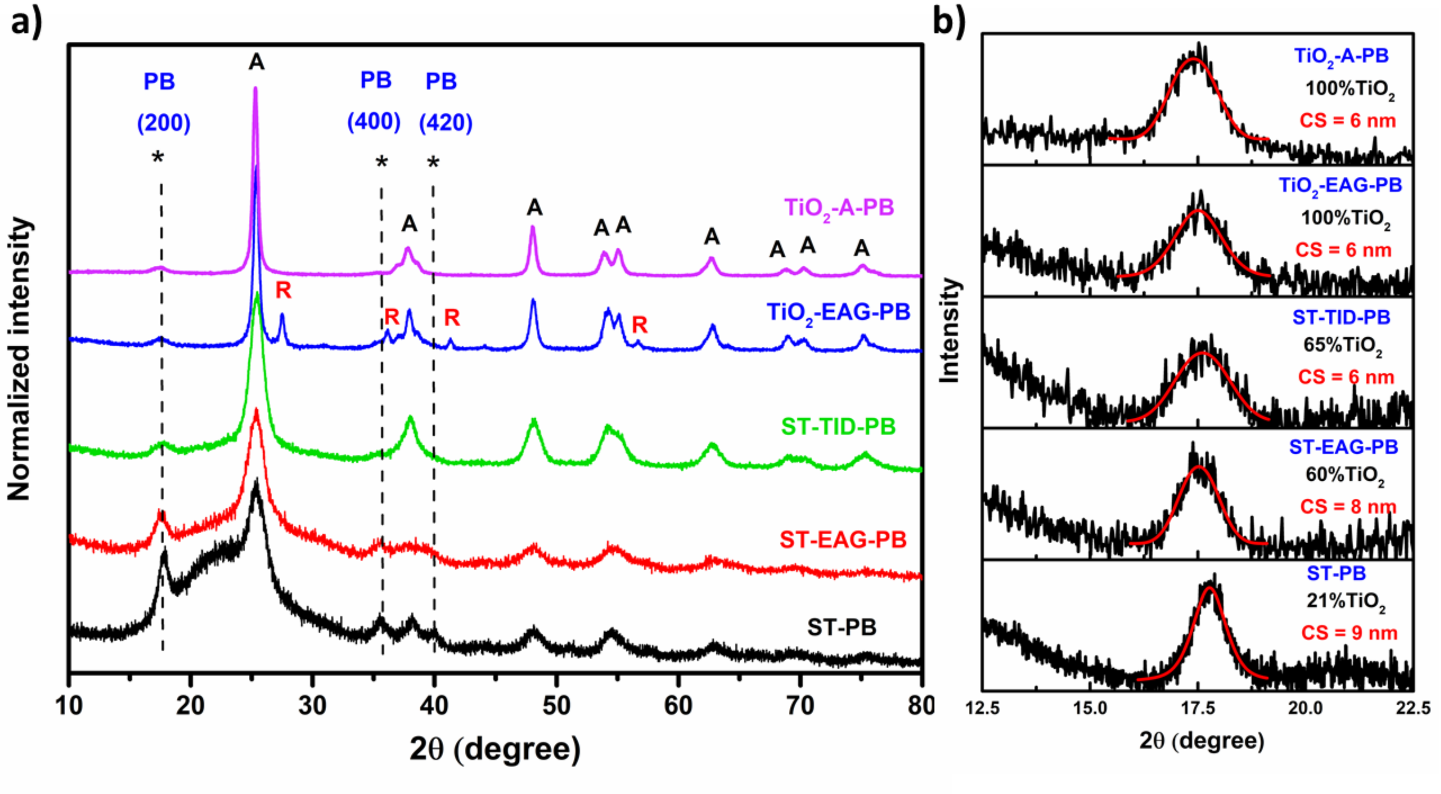

Figure 4. a) X-ray diffractograms of silica-titania and pure titania photocatalysts modified containing similar amounts of PB; (b) X-ray diffraction peaks corresponding to the crystalline plane (200) of the photodeposited PB in the different samples. For a better visualization of the diffraction peak and measurement of the crystallite size (CS) of the photo deposited PB, a baseline correction and peaks fitting were performed using the Pseudo-Voigt function (red curves, in (b)).

Diffraction peaks clear and intense enough to allow calculation of the crystallite size of PB were only observed in samples with higher (> 6% Fe) PB loading (PB3-series) (Fig. 4c). The crystallite sizes calculated based on the width of the (200) diffraction plane of PB using Scherrer formula varied between 6 and 9 nm, indicating the nanocrystalline nature of the photodeposited PB. A slight decrease in PB crystallite size with increase in %TiO_2 loading of the samples was observed (Fig. 4c). This behavior may be related to the high affinity of the titania surface for the $[Fe(CN)_6]^{-4}$ ions, which bind to the surface of TiO_2-based materials by chemisorption involving Ti(IV)–CN–Fe(II) bridging bonds [47]. This chemisorption process may promote greater dispersion of these adsorbed species (which act as nucleation sites for the formation of PB nanocrystallites) on the surface of TiO_2. A higher TiO_2 content of the silica-titania materials is then expected to result in a greater number of nucleation sites of the PB, leading to a decrease in the final crystallite size at the end of photodeposition process.

3.1.5 Morphogical study using eletron microscopy (SEM and TEM analysis)

Among the TiO_2-based photocatalysts studied in this work, the SiO_2@TiO_2 core@shell particles (ST series) have the most regular and uniform morphology. These particles were thus selected to evaluate the effect of PB deposition on the microstructure and morphology of the photocatalysts and to verify if PB is essentially deposited on their surfaces. Figs. 5 and 6 compare the SEM and TEM micrographs of a representative ST sample before and after photodeposition of PB. An analysis of the SEM images of ST and ST-PB2 samples indicates that both materials have a similar morphology, with only a subtle change in morphology induced by the incorporation of PB (Figs. 5a,b).

It is important to note that no free or isolated PB nanoparticles can be seen in these images, suggesting that PB is essentially and selectively deposited on the surface of the photocatalysts by heterogeneous nucleation and no precipitation as a result of homogenous nucleation in solution occurs. A closer look at the higher magnification SEM images (Figs. 5c and 5d) indicates that the surface texture of the particles undergoes a slight change after the photodeposition process, with the PB-modified particles (ST-PB2) appearing to be somewhat smoother and slightly bigger than unmodified ST particles.

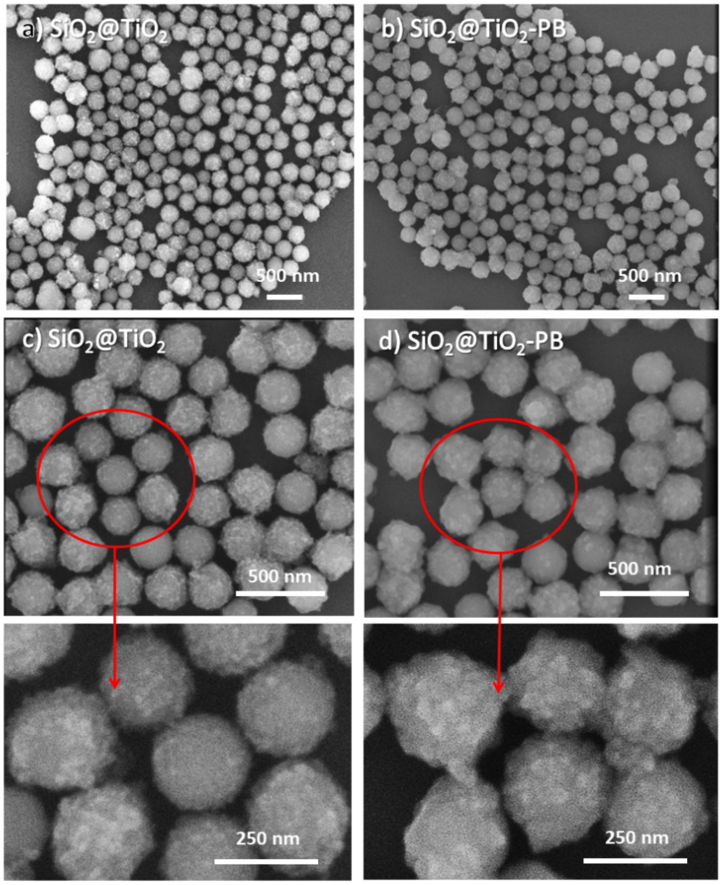

Figure 5. FEG-SEM images of (a,c) pristine ST core-shell particles in low (a) and higher (c) magnification, and (b,d) PB-modified sample (ST-PB2) in low (b) and high magnification (d). The bottom part of the Figure shows the magnified views of the encircled regions of each sample.

The TEM images of ST ($SiO_2@TiO_2$) particles clearly indicates the formation of a TiO_2 shell consisting of small nanoparticles around SiO_2 sub-micron particles, resulting in a core@shell structure. A comparison of the TEM macrographs of ST and ST-PB3 samples (Fig. 6) reveals that the shell part of ST core@shell particles becomes denser and thicker after modification with PB and the individual titania nanoparticles observable in ST sample (Figs. 6a,c) are less visible in ST-PB3 sample (Figs. 6b,d). This is probably due to the formation of a second PB layer around the titania nanocrystals in the shell part of ST particle, leading to the formation of $SiO_2@TiO_2@PB$ core@shell@shell architecture. Previous studies on TiO_2-PB composites have also suggested that PB tends to deposit itself in the form of thin layers on the surface of titania particles [27,29]. The higher magnification TEM image (Figs. 6d,e) appear to show the formation of such a PB overlay on the surface of the ST particles. Finally, the EDS microanalysis indicated the presence of Fe, Ti and Si in these PB-modified ST particles (ST-PB3), further confirming the successful deposition of PB on the surface of ST core@shell particles.

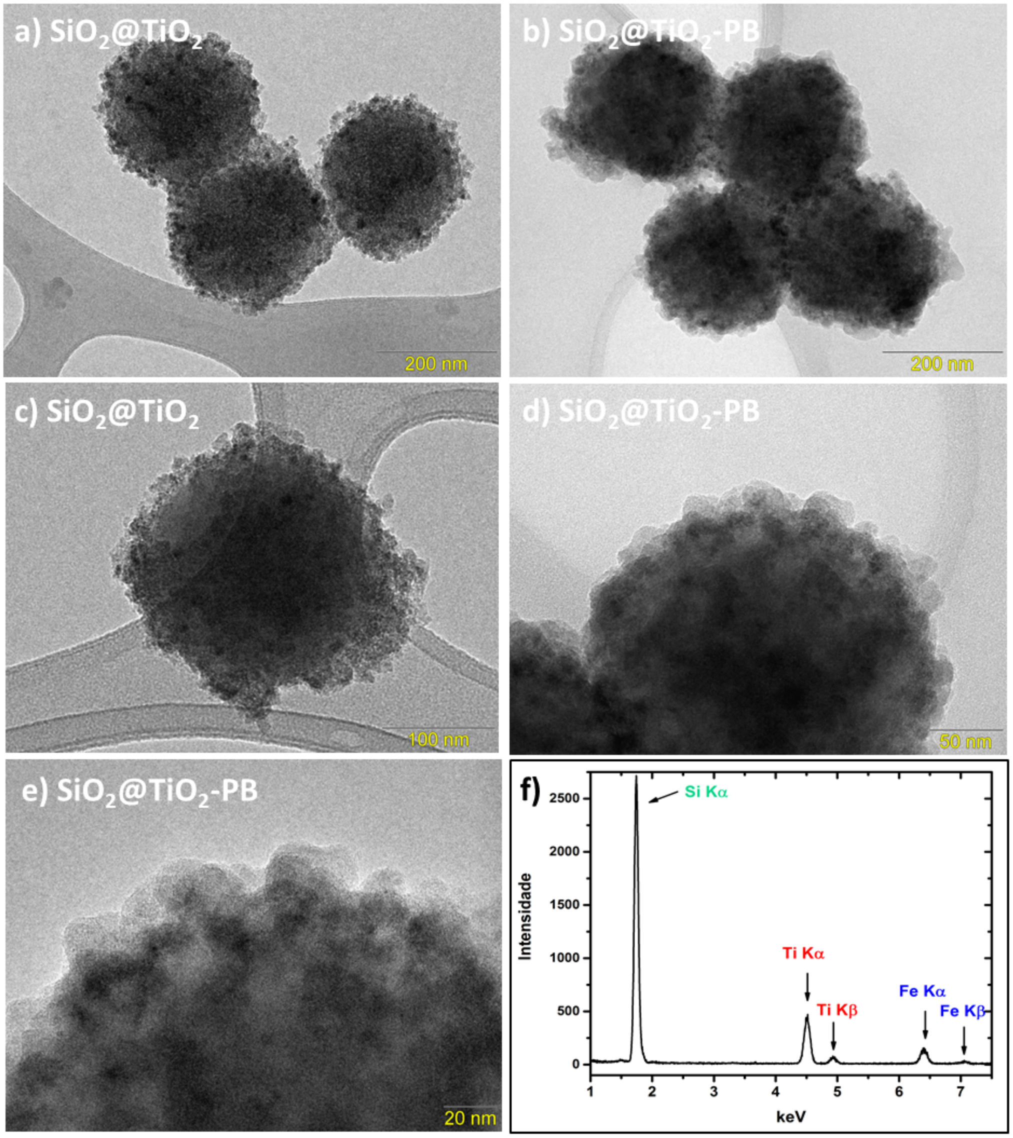

Figure 6. TEM images of (a,c) pristine ST core-shell particles in low (a) and higher (c) magnification, and (b,d) PB-modified sample (ST-PB3) in low (b) and higher magnification (d,e); (f) The EDS spectrum of the same ST-PB3 sample.

3.1.6 N_2 adsorption

The N_2 adsorption-desorption isotherms of SiO_2@TiO_2 core@shell particles (ST series), TiO_2 anatase nanoparticles, silica-titania aerogels (ST-TID and ST-EAG series) and titania aerogels (TiO_2-EAG) are shown in fig. 7, while textural properties values determined using BET method are summarized on table 2. The N_2 adsorption isotherms of ST series, TiO_2-A and TiO_2-A-PB can be classified as type IV in the general IUPAC classification [40], which are characteristic of mesoporous materials and thus confirm that the mesoporous nature of TiO_2 shell (ST series) are maintained even after photodeposition of PB. The desorption isotherms obtained for ST series, TiO_2-A and TiO_2-A-PB samples has a hysteresis that resembles that of type H4 and H3 according to the general classification of IUPAC [40], which characterizes solids that consist of aggregates or agglomerates of particles forming slit-shaped pores, cones and/or parallel plates whose sizes are uniform and nonuniform respectively. The photodeposition of PB on surface of these materials implies on slightly increases of S_{BET} and V_p while I_p decreases in agreement. This can be attributed to the formation of a second PB thin layer around the titania nanocrystals in the shell part of ST particle as discussed in TEM analysis. This is corroborated with the PSD curves that showed an increase in the incremental pore volume and the appearance of pore classes in the mesoporous region around 20 nm related to TiO_2 shell in SiO_2@TiO_2 particles.

Different textural properties of the TiO_2-EAG series and between two different silica-titania aerogels imply differentiated deposition of Prussian Blue in the network that compose these materials. The N_2 adsorption curves of silica-titania aerogels (ST-TID and ST-EAG series) and titania aerogels (TiO_2-EAG) can be classified as a type IV isotherms [40], confirming that mesoporous characteristic of porous nature of the aerogels are preserved after surface modification with PB. The N_2 desorption curves obtained from ST-TID, ST-TID-PB2, TiO_2-EAG and TiO_2-EAG-PB2 aerogels can be classified as a type H1, which characterizes uniform cylindrical mesopores shape formed by aggregates and or clusters of spheroidal particles [40]. ST-EAG series desorption isotherms depict hysteresis better classified as H3 type, which characteristic of non-uniform slit-shaped pores [40,48]. The surface area (S_{BET}) for the TiO_2-EAG series increased slightly after photodeposition of PB, while V_p and I_p values decreases, probably because the thin layer of PB is formed on solid TiO_2 network filling the mesopores that make up the material, this effect can be observed in the PSD curves, the incorporation of PB in the structure of TiO_2-EAG aerogels shift toward the mesopores, giving rise to new classes of pores. ST-TID and ST-EAG aerogels series shown the typical values from S_{BET}, V_p and I_p. Nevertheless, slight differences are observed between the two different silica-titania aerogels at structural parameters after photodeposition of PB. The porosity and average pore size increase for both materials, however, the S_{BET} obtained for ST-EAG-PB2 decreases. This discrepancy could be explained on the basis of the observation that conventional nitrogen adsorption method applied can seriously underestimate the macropores region. Such inference is further supported by pore size distribution (PSD) analysis of the ST-TID and ST-EAG aerogels which shown the multimodal pore distribution on the mesopore and macropore regions. The pore size distribution curves of the silica-titania aerogels shift toward the mesopore region after surface modification with PB, suggesting that overall photodeposition process results in a significative changes of silica-titania network porosity.

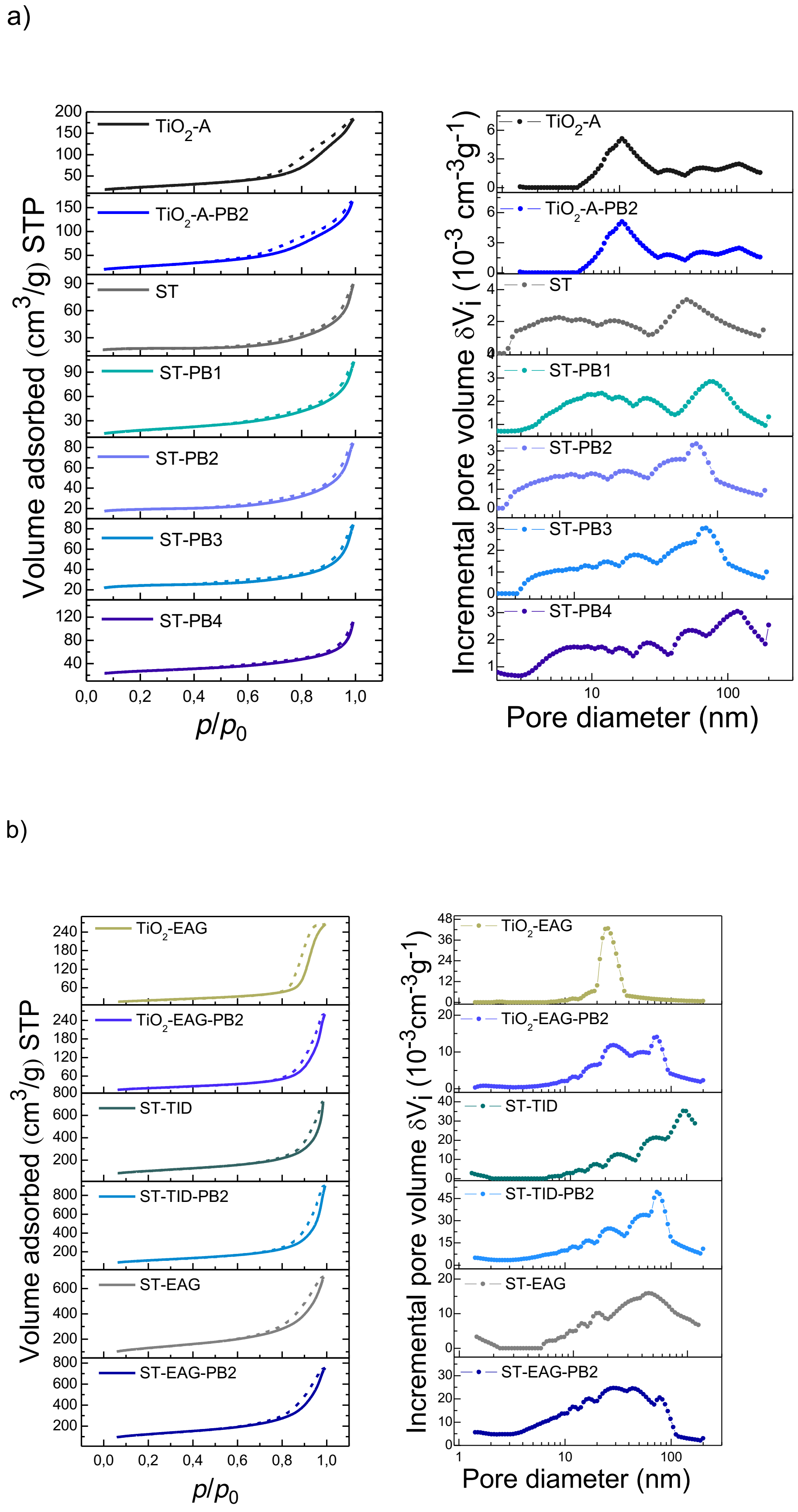

Figure 7. N_2 adsorption-desorption isotherms of a) ST, ST-PB samples with different PB loadings, TiO_2 and TiO_2-PB particles b) different silica-titania aerogels, titania aerogels without PB and modified containing similar amounts of PB.

Table 2. Textural parameters obtained from N_2 adsorption and BET method for the ST series, TiO_2 particles, different silica-titania aerogels and titania aerogels.

Sample	S_{BET} ($m^2.g^{-1}$)	V_p ($cm^3.g^{-1}$)	l_p (nm)
ST	62 (1)	0.12	7.9
ST-PB1	66 (1)	0.14	8.6
ST-PB2	66 (1)	0.12	7.2
ST-PB3	83 (2)	0.12	5.7
ST-PB4	94 (1)	0.15	6.3
ST-EAG	465 (2)	1.04	8.9
ST-EAG-PB2	446 (2)	1.12	10.1
ST-TID	369 (2)	0.97	10.6
ST-TID-PB2	391 (2)	1.22	12.5
TiO_2-EAG	70 (1)	0.41	23.6
TiO_2-EAG-PB2	78 (1)	0.36	18.6
TiO_2-A	86 (1)	0.27	12.4
TiO_2-A-PB2	96 (1)	0.23	9.7

3.2. Cr (VI) photocatalytic reduction

The photocatalytic reduction of Cr(VI) to Cr(III) in the presence of different silica-titania and PB-modified silica-titania photocatalysts (ST and STPB samples) was carried out to evaluate the role of PB in the photocatalytic activity of these samples. Importantly, no solution pH adjustment was employed during the photocatalytic tests and the tests were carried out at natural unadjusted pH of around 5.6. The decrease in concentration of Cr(VI) was monitored by measuring the change in absorbance ($\lambda_{max.}$ = 545 nm) of Cr(VI)-DPC complex (see the digital photos in inset of Fig.8a, also) as a function of UV illumination time (Figure 8a). Figure 8b and 8c compare the kinetic profiles and photocatalytic Cr(VI) reduction efficiency after 60 minutes of UV irradiation (Figure 8c), respectively, for ST and ST-PB samples containing different amounts of PB. The Cr(VI) photoreduction efficiency of unmodified ST is low and these samples could reduce only 31±5% of Cr(VI) within 1h of UV illumination, as compared to 65–85% reduction observed in case of PB-modified ST-PB samples.

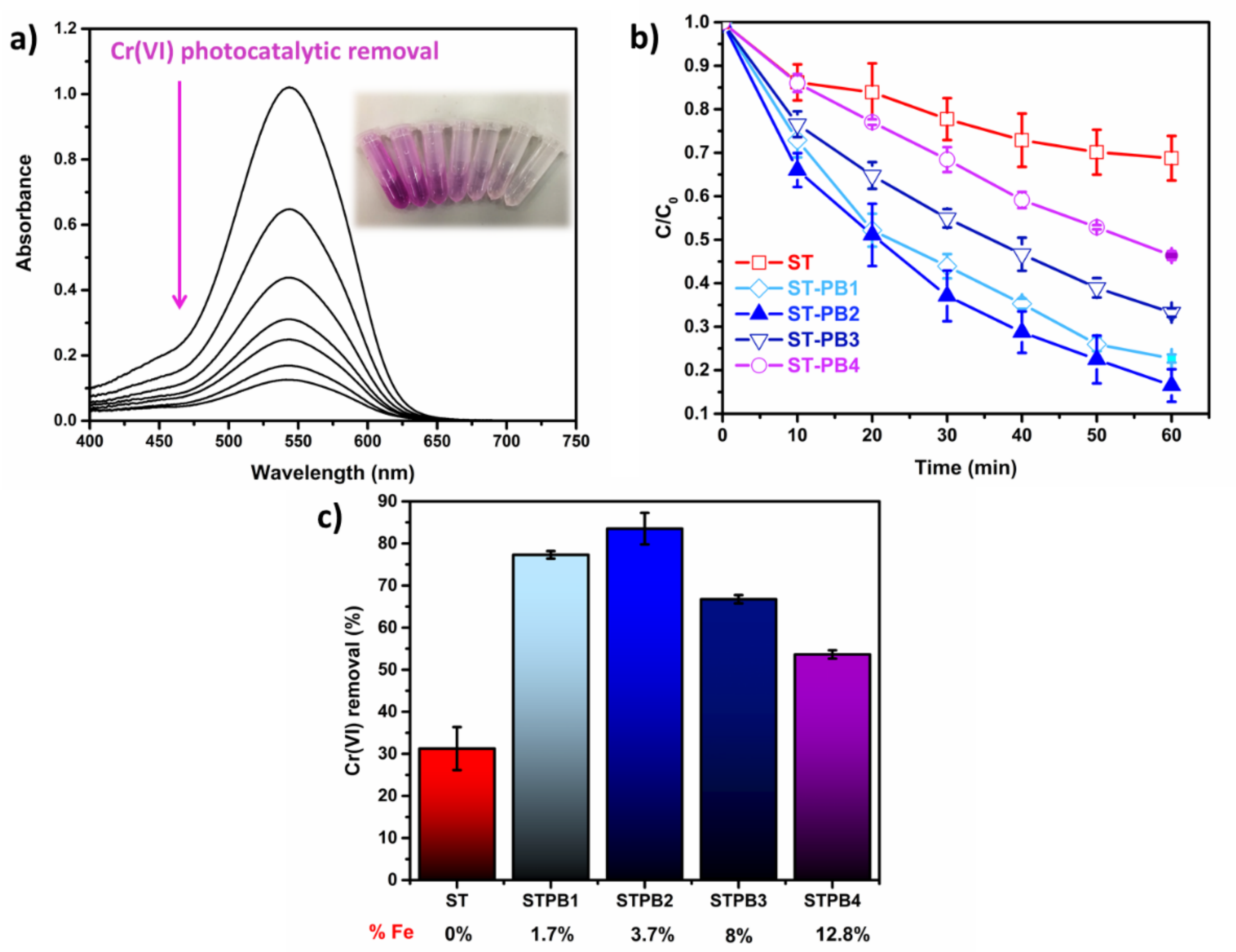

Figure 8. (a) Visible absorption spectrum of Cr(VI)-DPC complex showing the decrease in Cr(VI) content of the reaction mixture as a function of UV illumination time due to photocatalytic reduction of Cr(VI) to Cr(III) on the surface of SiO_2@TiO_2-PB particles (ST-PB2 sample); A comparison of the (b) kinetic profiles and (c) photocatalytic Cr(VI) reduction efficiency of unmodified (ST) and PB-modified ST samples (ST-PB series). The inset in are digital photos of Cr(VI)-DPC complex obtained after different UV illumination intervals in the presence of ST-PB2 photocatalysts. Conditions: Cr(VI) = 10 mg. L^{-1}, pH = 5.6 (unadjusted).

Previous studies of Cr(VI) photoreduction by unmodified TiO_2 and other semiconductors have also reported a low efficiency of the process [11,12,49] and there are several factors responsible for this. These studies demonstrate that the photocatalytic reduction of Cr(VI) to Cr(III) is less efficient and slow in deionized water (less acidic medium) and in the absence of organic species that can act as electron donors (or hole scavengers). In the absence of such easily oxidizable species, the other possible oxidation reaction, occurring concomitantly with Cr(VI) reduction, is the oxidation of water which is kinetically unfavorable and slow [12,49]. The Cr(VI) reduction reaction is much more efficient in acidic environment as it involves participation of a large number of protons on the reactant side, as shown below [11].

$$\text{Acidic media: } 2\ Cr_2O_7^{2-} + 16\ H^+ \rightarrow 4\ Cr^{3+} + 8\ H_2O + 3\ O_2$$

$$\text{Neutral media: } 4\ CrO_4^{2-} + 20\ H^+ \rightarrow 4\ Cr^{3+} + 10\ H_2O + 3\ O_2$$

Moreover, the reduction potential of chromate ion decreases with the pH of the medium, making it a more oxidizing species (more susceptible to reduction) in a more acidic medium [49,50]. Another factor that limits the efficiency of the photocatalytic reduction at higher pH values is the formation of $Cr(OH)_3$ as a product of the reduction reaction and its subsequent deposition on the surface of the photocatalysts, resulting in the progressive deactivation of the photocatalytic sites [51]. Considering the factors discussed above, it can thus be inferred that the efficiency of photoreduction of Cr(VI) using unmodified TiO_2 and SiO_2-TiO_2 materials is low, particularly in neutral or low acidic reaction media.

Modification of ST particles with PB leads to an enhancement of their photoreduction ability and higher Cr(VI) photoreduction efficiency (65–85%) was achieved for ST-PB samples (Figs. 8b,c). In general, all the PB-modified samples (ST-PB) exhibit better photocatalytic activity as compared to unmodified ST particles (31±5%). Among the ST-PB samples, ST-PB2 (3.7% Fe) shows the highest photoactivity, reducing 84±4% of Cr(VI) within 60 min of UV illumination, a value much superior to that achieved for unmodified ST (31±5%). Considering the PB loading in this sample as optimum, we then compared the photocatalytic activity of different SiO_2-TiO_2 and TiO_2 based aerogels and particles before and after modification with similar amount of PB (3–3.7% Fe) (Figs. 9,10). A general analysis of the results reveals that the unmodified SiO_2-TiO_2 and TiO_2 aerogels and particles show low photocatalytic activity towards reduction of Cr (VI) (20–40% reduction) under the conditions employed and incorporation of PB in all of these samples leads to a significant improvement in the photocatalytic response (Fig. 9). A comparison of the photocatalytic activity (10a) and the first order kinetic constants (Figure 10b) of different SiO_2-TiO_2-PB materials (particles and aerogels) modified with similar amount of PB reveals similar photocatalytic activity for these different samples. Interestingly, the highest photocatalytic activity was observed for titania aerogels modified with PB (TiO_2-EAG-PB2 sample) which could reduce 97±1% and 100% of Cr(VI) within 30 min and 40 min of UV irradiation, respectively, in deionized water and in the total absence of organic electron donors, a remarkable photocatalytic performance.

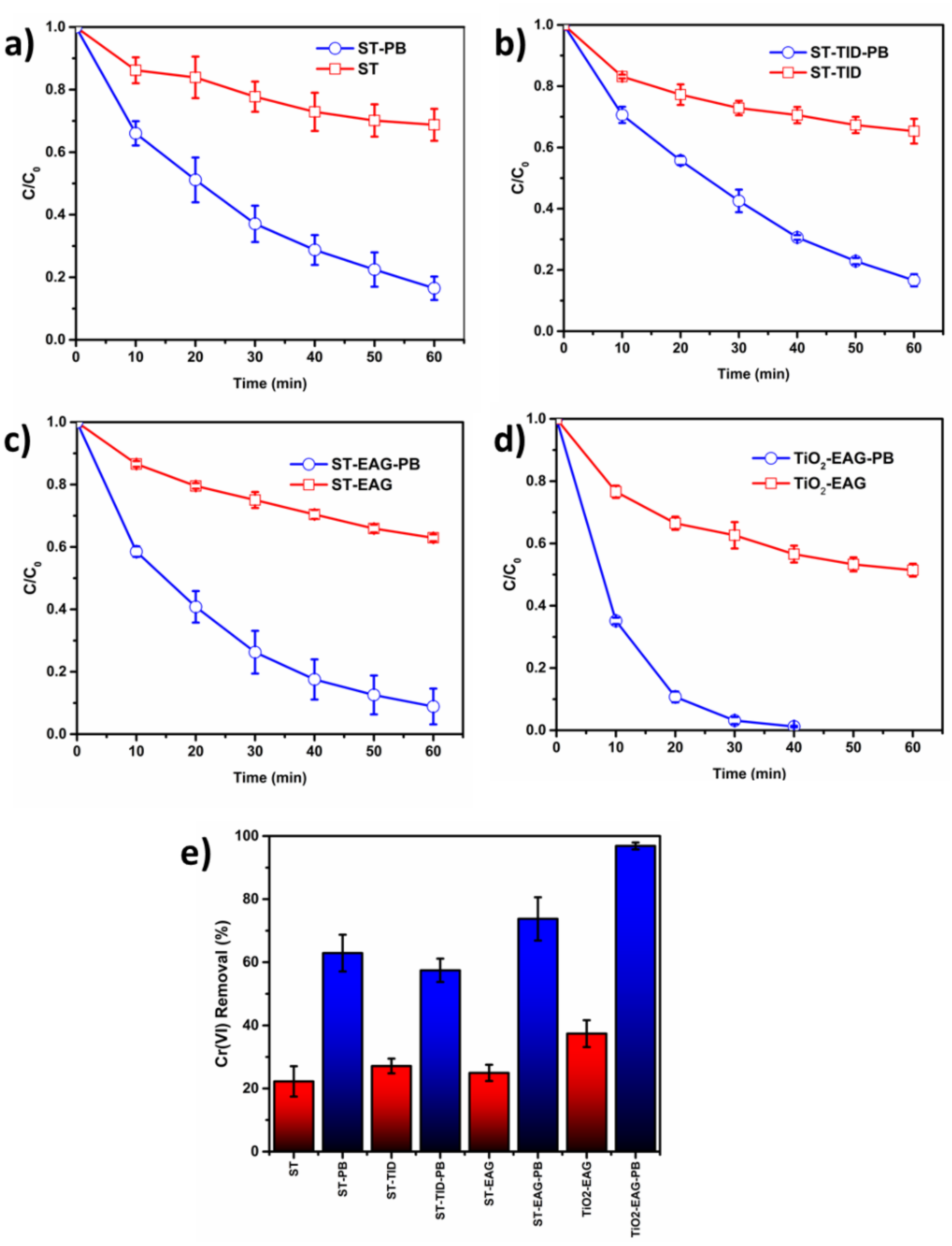

Figure 9. (a-d) Kinetic profiles showing a comparison of the photoactivity of titania and different silica-titania materials before and after modification with PB: (a) ST core@shell particles, (b) TID SiO_2@TiO_2 Aerogel, (c) EAG SiO_2@TiO_2 Aerogel, (d) EAG TiO_2 Aerogel; (e) comparison of the Cr(VI) photoreduction efficiency of different titania and silica-titania based photocatalysts with and without PB.

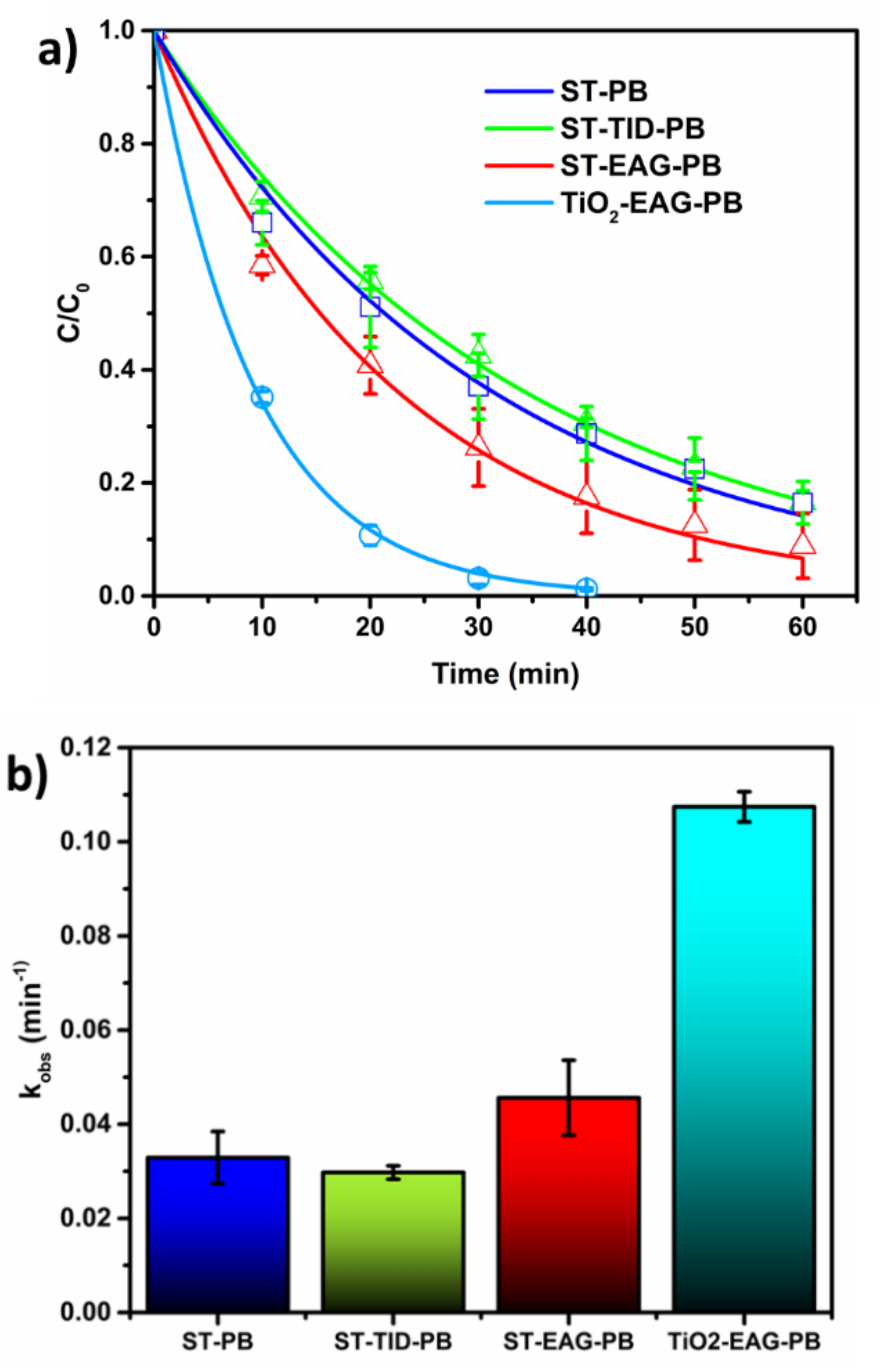

Figure 10. (a) Kinetic profiles and (b) first order kinetic constants for different SiO_2-TiO_2-PB2-type samples (particles and aerogels) modified with similar amount of PB (3-3.7% Fe).

Figure 11 illustrates proposed schemes to explain the improved photocatalytic activity of TiO_2-Prussian Blue-based photocatalysts. The superior photocatalytic activity of PB-modified samples can be attributed to the ability of the PB layer act as an electron mediator between the titania surface and the Cr(VI) species in solution (Figure 11a). The transfer of electrons from the conduction band of TiO_2 to PB leads to the formation of its reduced form, the Prussian white (PW), by reducing Fe (III) high-spin sites [30,52]. These reduced sites can, in turn, act as catalytic sites of reduction from Cr(VI) to Cr(III), with the efficiency of the process being increased as these high spin Fe (II) species have a lifetime longer than that of the photo-excited electrons in titania, thereby increasing the probability of electrons transfer to the ions in solution. A previous research study, involving glassy carbon/PB electrode, has in fact proved the electrocatalytic activity of PB towards reduction of Cr (VI) and the authors explored this effect for the development of electroanalytical sensors for the selective detection of very low Cr (VI) concentrations [36]. It is also worth mentioning that the efficient transfer of electrons from the conduction band of TiO_2 to the PB layer at the TiO_2-PB interface leads to an effective charge separation in TiO_2, thereby reducing surface recombination processes, and thus improving the photocatalytic efficiency of the material. Finally, the greater photocatalytic performance shown uniquely by TiO_2-EAG-PB sample suggest a possible synergistically effect between PB role as a co-catalyst and occurrence of bicrystalline anatase/rutile heterojunctions, thus further improving charge separation and overall photocatalytic performance (see Figure 11b). To the best of our knowledge, this is the first report on the ability of PB to act as a co-catalyst in photocatalytic reduction reactions promoted by titania-based catalysts.

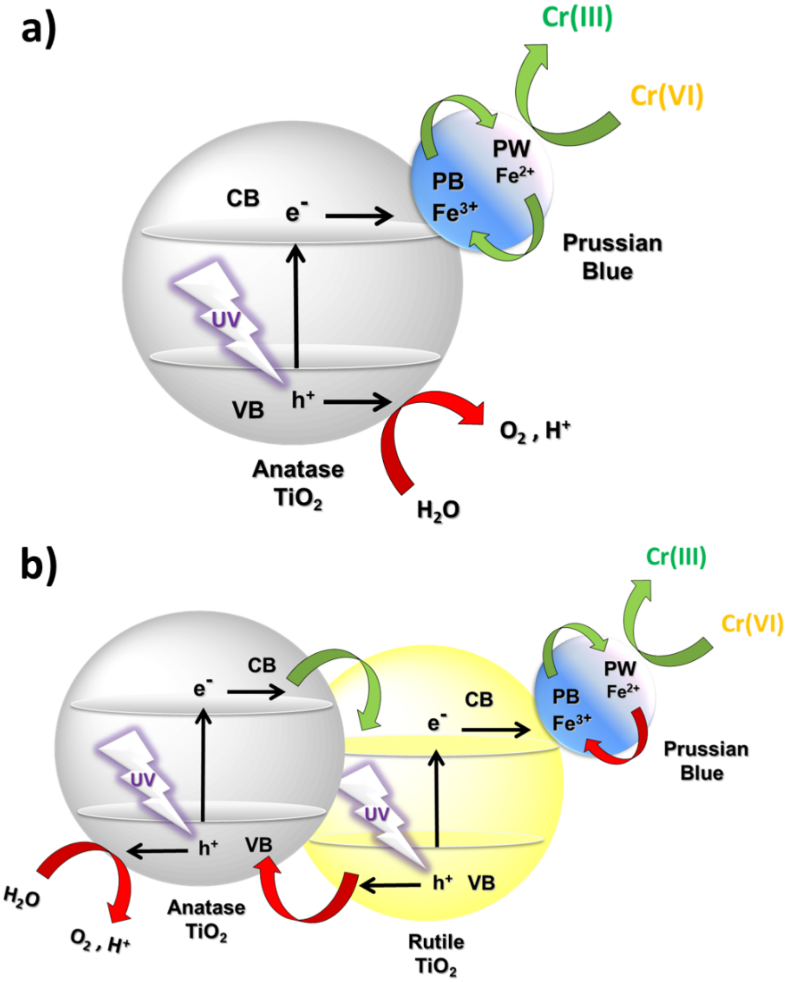

Figure 11. Illustrative scheme of proposed mechanism for enhanced photocatalytic by coupling of phase-pure Anatase (a) mixed Anatase/Rutile heterojunction (b) TiO_2 photocatalysts to Prussian Blue co-catalyst. PB stands for “Prussian Blue”, while PW stands for “Prussian White”, its reduced form.

4. Conclusions

In this study, we explored, for the first time, the role of Prussian Blue (PB) as a co-catalyst to improve the photocatalytic properties of TiO_2 and SiO_2-TiO_2 based materials towards photoreduction of Cr(VI). The base photocatalysts particles (TiO_2 and core@shell SiO_2@TiO_2) and aerogels (TiO_2, core@shell SiO_2@TiO_2 and mixed SiO_2@TiO_2) were coated with different amounts (1.7–12.8% Fe) of nanocrystalline PB using a very reproducible photodeposition method. The formation of PB was confirmed by SEM, XRD and vibrational spectroscopy characterization. For a given irradiation time (1h) and precursors ($K_3[Fe(CN)_6]$, $Fe(NO_3)_3$) concentration, the %Fe loading of different TiO_2-materials mentioned above was almost similar (Fe= 3–3.7%), indicating that the amount of photodeposited PB does not vary significantly with the type or chemical composition of titania or silica-titania based photocatalysts. The Cr(VI) photoreduction tests demonstrated that all the PB-modified photocatalysts (both aerogels and particles) possess higher photocatalytic activity than the respective unmodified photocatalysts. Among the PB-modified photocatalysts, the PB-photocatalysts aerogels exhibited higher photocatalytic activity than the respective PB-nanoparticle samples. Remarkably, this occured in deionized water and in the absence of electron donor (hole scavenger) organic molecules. Moreover, the photocatalytic activity of the samples was dependent on the PB loading and samples with 3–3.7% Fe (PB2 series) exhibit the highest photoactivity (85–100% Cr(VI) photoreduction in 1h) as compared to unmodified photocatalysts (20–40% reduction). Considering the ease with which PB can be incorporated, *via* photodeposition method, onto the surface of several classes of photocatalysts, including TiO_2, we believe that the work described herein opens up new possibilities for the preparation of several other photocatalyst/PB systems with improved photocatalytic activities towards Cr (VI) reduction and other target applications.

5. Acknowledgements

This work was supported by São Paulo Research Foundation (FAPESP) [research grants no. 2013/24948-3, 2015/22828-6, 2016/10939-0, 2018/01934-0 and 2018/19785-1]. This work was also partially performed under the auspices of the U.S. Department of Energy by Lawrence Livermore National Laboratory under Contract DEAC52-07NA27344. Elias P. Ferreira-Neto thanks FAPESP for PhD and post-doctoral fellowships [grants # 2013/24948-3 and # 2018/01934-0]. S. Ullah acknowledges financial support from Higher Education Commission, Pakistan [Project No. 9286]. The authors acknowledge the Brazilian funding agencies (CNPq and CAPES) for financial assistance. Amanda P. Perissinotto thank the Coordination for the Improvement of Higher Education Personnel (CAPES, Brazil) for PhD fellowship.

6. References:

[1] L. Rizzo, S. Malato, D. Antakyali, V.G. Beretsou, M.B. Đolić, W. Gernjak, E. Heath, I. Ivancev-Tumbas, P. Karaolia, A.R. Lado Ribeiro, G. Mascolo, C.S. McArdell, H. Schaar, A.M.T. Silva, D. Fatta-Kassinos, Consolidated vs new advanced treatment methods for the removal of contaminants of emerging concern from urban wastewater, Sci. Total Environ. 655 (2019) 986–1008. https://doi.org/https://doi.org/10.1016/j.scitotenv.2018.11.265.

[2] P. Borah, M. Kumar, P. Devi, Chapter 2 - Types of inorganic pollutants: metals/metalloids, acids, and organic forms, in: P. Devi, P. Singh, S.K.B.T.-I.P. in W. Kansal (Eds.), Elsevier, 2020: pp. 17–31. https://doi.org/https://doi.org/10.1016/B978-0-12-818965-8.00002-0.

[3] C.F. Carolin, P.S. Kumar, A. Saravanan, G.J. Joshiba, M. Naushad, Efficient techniques for the removal of toxic heavy metals from aquatic environment: A review, J. Environ. Chem. Eng. 5 (2017) 2782–2799. https://doi.org/https://doi.org/10.1016/j.jece.2017.05.029.

[4] J.J. Coetzee, N. Bansal, E.M.N. Chirwa, Chromium in Environment, Its Toxic Effect from Chromite-Mining and Ferrochrome Industries, and Its Possible Bioremediation, Expo. Heal. 12 (2020) 51–62. https://doi.org/10.1007/s12403-018-0284-z.

[5] M. Nur-E-Alam, M.A.S. Mia, F. Ahmad, M.M. Rahman, An overview of chromium removal techniques from tannery effluent, Appl. Water Sci. 10 (2020) 205. https://doi.org/10.1007/s13201-020-01286-0.

[6] C. He, L. Gu, Z. Xu, H. He, G. Fu, F. Han, B. Huang, X. Pan, Cleaning chromium pollution in aquatic environments by bioremediation, photocatalytic remediation, electrochemical remediation and coupled remediation systems, Environ. Chem. Lett. 18 (2020) 561–576. https://doi.org/10.1007/s10311-019-00960-3.

[7] S.K. Loeb, P.J.J. Alvarez, J.A. Brame, E.L. Cates, W. Choi, J. Crittenden, D.D. Dionysiou, Q. Li, G. Li-Puma, X. Quan, D.L. Sedlak, T. David Waite, P. Westerhoff, J.-H. Kim, The Technology Horizon for Photocatalytic Water Treatment: Sunrise or Sunset?, Environ. Sci. Technol. 53 (2019) 2937–2947. https://doi.org/10.1021/acs.est.8b05041.

[8] B. Ohtani, Revisiting the fundamental physical chemistry in heterogeneous photocatalysis: its thermodynamics and kinetics, Phys. Chem. Chem. Phys. 16 (2014) 1788–1797. https://doi.org/10.1039/C3CP53653J.

[9] M.I. Litter, Mechanisms of removal of heavy metals and arsenic from water by TiO2-heterogeneous photocatalysis, Pure Appl. Chem. 87 (2015) 557–567. https://doi.org/10.1515/pac-2014-0710.

[10] Z. Zhao, H. An, J. Lin, M. Feng, V. Murugadoss, T. Ding, H. Liu, Q. Shao, X. Mai, N. Wang, H. Gu, S. Angaiah, Z. Guo, Progress on the Photocatalytic Reduction Removal of Chromium Contamination, Chem. Rec. 19 (2019) 873–882. https://doi.org/https://doi.org/10.1002/tcr.201800153.

[11] Q. Cheng, C. Wang, K. Doudrick, C.K. Chan, Hexavalent chromium removal using metal oxide photocatalysts, Appl. Catal. B Environ. 176–177 (2015) 740–748. https://doi.org/http://dx.doi.org/10.1016/j.apcatb.2015.04.047.

[12] L. Wang, N. Wang, L. Zhu, H. Yu, H. Tang, Photocatalytic reduction of Cr(VI) over different TiO2

photocatalysts and the effects of dissolved organic species, J. Hazard. Mater. 152 (2008) 93–99. https://doi.org/http://dx.doi.org/10.1016/j.jhazmat.2007.06.063.

[13] K.H. and H.I. and A. Fujishima, TiO 2 Photocatalysis: A Historical Overview and Future Prospects, Jpn. J. Appl. Phys. 44 (2005) 8269. http://stacks.iop.org/1347-4065/44/i=12R/a=8269.

[14] K. Nakata, A. Fujishima, TiO2 photocatalysis: Design and applications, J. Photochem. Photobiol. C Photochem. Rev. 13 (2012) 169–189. https://doi.org/http://dx.doi.org/10.1016/j.jphotochemrev.2012.06.001.

[15] K. Suttiponparnit, J. Jiang, M. Sahu, S. Suvachittanont, T. Charinpanitkul, P. Biswas, Role of Surface Area, Primary Particle Size, and Crystal Phase on Titanium Dioxide Nanoparticle Dispersion Properties, Nanoscale Res Lett. 6 (2010) 1–8. https://doi.org/10.1007/s11671-010-9772-1.

[16] F. Pellegrino, L. Pellutiè, F. Sordello, C. Minero, E. Ortel, V.-D. Hodoroaba, V. Maurino, Influence of agglomeration and aggregation on the photocatalytic activity of TiO2 nanoparticles, Appl. Catal. B Environ. 216 (2017) 80–87. https://doi.org/https://doi.org/10.1016/j.apcatb.2017.05.046.

[17] D. a. H. Hanaor, C.C. Sorrell, Review of the anatase to rutile phase transformation, J. Mater. Sci. 46 (2011) 855–874. https://doi.org/10.1007/s10853-010-5113-0.

[18] B. Ohtani, Titania Photocatalysis beyond Recombination: A Critical Review, Catalysts. 3 (2013) 942–953. https://doi.org/10.3390/catal3040942.

[19] M. Pelaez, N.T. Nolan, S.C. Pillai, M.K. Seery, P. Falaras, A.G. Kontos, P.S.M. Dunlop, J.W.J. Hamilton, J.A. Byrne, K. O'Shea, M.H. Entezari, D.D. Dionysiou, A review on the visible light active titanium dioxide photocatalysts for environmental applications, Appl. Catal. B Environ. 125 (2012) 331–349. https://doi.org/10.1016/j.apcatb.2012.05.036.

[20] H. Wang, L. Zhang, Z. Chen, J. Hu, S. Li, Z. Wang, J. Liu, X. Wang, Semiconductor heterojunction photocatalysts: design, construction, and photocatalytic performances, Chem. Soc. Rev. 43 (2014) 5234–5244. https://doi.org/10.1039/C4CS00126E.

[21] M. Dahl, Y. Liu, Y. Yin, Composite Titanium Dioxide Nanomaterials, Chem. Rev. 114 (2014) 9853–9889. https://doi.org/10.1021/cr400634p.

[22] A. Ludi, Prussian blue, an inorganic evergreen, J. Chem. Educ. 58 (1981) 1013. https://doi.org/10.1021/ed058p1013.

[23] M. Ware, Prussian Blue: Artists' Pigment and Chemists' Sponge, J. Chem. Educ. 85 (2008) 612. https://doi.org/10.1021/ed085p612.

[24] K. Dunbar, R. Heintz, Chemistry of transition metal cyanide compounds: modern perspectives, Prog. Inorg. Chem. 45 (1997) 283–391. http://books.google.com/books?hl=en&lr=&id=2TFQ92RnkQ0C&oi=fnd&pg=PA283&dq=Chemistry+of+Transition+Metal+Cyanide+Compounds+:+Modern+Perspectives&ots=2KH3WJHaxU&sig=abSRuPaL_-BlLIsYMnZhMKBlL5A (accessed November 19, 2013).

[25] L.-M. Cao, D. Lu, D.-C. Zhong, T.-B. Lu, Prussian blue analogues and their derived nanomaterials for electrocatalytic water splitting, Coord. Chem. Rev. 407 (2020) 213156. https://doi.org/https://doi.org/10.1016/j.ccr.2019.213156.

[26] J. Chen, L. Wei, A. Mahmood, Z. Pei, Z. Zhou, X. Chen, Y. Chen, Prussian blue, its analogues and their derived materials for electrochemical energy storage and conversion, Energy Storage Mater. 25 (2020) 585–612. https://doi.org/https://doi.org/10.1016/j.ensm.2019.09.024.

[27] K. Szaci?owski, W. Macyk, G. Stochel, Synthesis, structure and photoelectrochemical properties of the TiO2?Prussian blue nanocomposite, J. Mater. Chem. 16 (2006) 4603–4611. https://doi.org/10.1039/b606402g.

[28] B. Seelandt, M. Wark, Electrodeposited Prussian Blue in mesoporous TiO2 as electrochromic hybrid material, Microporous Mesoporous Mater. 164 (2012) 67–70. https://doi.org/http://dx.doi.org/10.1016/j.micromeso.2012.06.015.

[29] H. Tada, Y. Saito, H. Kawahara, Photodeposition of Prussian Blue on TiO2 Particles, J. Electrochem. Soc. 138 (1991) 140–144. http://jes.ecsdl.org/content/138/1/140.short (accessed November 19, 2013).

[30] T. Yamamoto, N. Saso, Y. Umemura, Y. Einaga, Photoreduction of Prussian Blue intercalated into titania nanosheet ultrathin films., J. Am. Chem. Soc. 131 (2009) 13196–7. https://doi.org/10.1021/ja9041274.

[31] L. Han, L. Bai, S. Dong, Self-powered visual ultraviolet photodetector with Prussian blue electrochromic display, Chem. Commun. 50 (2014) 802–804. https://doi.org/10.1039/C3CC47080F.

[32] X. Li, J. Wang, A.I. Rykov, V.K. Sharma, H. Wei, C. Jin, X. Liu, M. Li, S. Yu, C. Sun, D.D. Dionysiou, Prussian blue/TiO2 nanocomposites as a heterogeneous photo-Fenton catalyst for degradation of organic pollutants in water, Catal. Sci. Technol. 5 (2015) 504–514. https://doi.org/10.1039/C4CY00947A.

[33] S. Husmann, L.F. Lima, L.S. Roman, A.J.G. Zarbin, Photoanode for Aqueous Dye-Sensitized Solar Cells based on a Novel Multicomponent Thin Film, ChemSusChem. 11 (2018) 1238–1245. https://doi.org/https://doi.org/10.1002/cssc.201702218.

[34] H. Kim, M. Kim, W. Kim, W. Lee, S. Kim, Photocatalytic enhancement of cesium removal by Prussian blue-deposited TiO2, J. Hazard. Mater. 357 (2018) 449–456. https://doi.org/https://doi.org/10.1016/j.jhazmat.2018.06.037.

[35] R. Chen, Q. Zhang, Y. Gu, L. Tang, C. Li, Z. Zhang, One-pot green synthesis of Prussian blue nanocubes decorated reduced graphene oxide using mushroom extract for efficient 4-nitrophenol reduction, Anal. Chim. Acta. 853 (2015) 579–587. https://doi.org/https://doi.org/10.1016/j.aca.2014.10.049.

[36] S. Xing, H. Xu, G. Shi, J. Chen, L. Zeng, L. Jin, A Simple and Sensitive Method for the Amperometric Detection of Trace Chromium(VI) Based on Prussian Blue Modified Glassy Carbon Electrode, Electroanalysis. 21 (2009) 1678–1684. https://doi.org/10.1002/elan.200904594.

[37] E.P. Ferreira-Neto, S. Ullah, M.B. Simões, A.P. Perissinotto, F.S. de Vicente, P.-L.M. Noeske, S.J.L. Ribeiro, U.P. Rodrigues-Filho, Solvent-controlled deposition of titania on silica spheres for the preparation of SiO2@TiO2 core@shell nanoparticles with enhanced photocatalytic activity, Colloids Surfaces A Physicochem. Eng. Asp. 570 (2019) 293–305. https://doi.org/https://doi.org/10.1016/j.colsurfa.2019.03.036.

[38] E.P. Ferreira-Neto, M.A. Worsley, U.P. Rodrigues-Filho, Towards thermally stable aerogel photocatalysts: $TiCl_4$-based sol-gel routes for the design of nanostructured silica-titania aerogel with high photocatalytic activity and outstanding thermal stability, J. Environ. Chem. Eng. 7 (2019) 103425. https://doi.org/https://doi.org/10.1016/j.jece.2019.103425.

[39] E.P. Ferreira Neto, S. Ullah, V.P. Martinez, J.M.S.C. Yabarrena, M.B. Simões, A.P. Perissinotto, H. Wender, F.S. de Vicente, M. Noeske, S.J.L. Ribeiro, U.P. Rodrigues-Filho, Thermally stable SiO2@TiO2 core@shell nanoparticles for application in photocatalytic self-cleaning ceramic tiles, Mater. Adv. (2021). https://doi.org/10.1039/D0MA00785D.

[40] G. Leofanti, M. Padovan, G. Tozzola, B. Venturelli, Surface area and pore texture of catalysts, Catal. Today. 41 (1998) 207–219. https://doi.org/http://dx.doi.org/10.1016/S0920-5861(98)00050-9.

[41] T. Matthias, K. Katsumi, N.A. V, O.J. P, R.-R. Francisco, R. Jean, S.K.S. W, Physisorption of gases, with special reference to the evaluation of surface area and pore size distribution (IUPAC Technical Report), Pure Appl. Chem. 87 (2015) 1051. https://doi.org/10.1515/pac-2014-1117.

[42] K. Ueno, T. Imamura, K.L. Cheng, Handbook of Organic Analytical Reagents, 2^a, CRC Press, 1992.

[43] S.F.A. Kettle, E. Diana, E.M.C. Marchese, E. Boccaleri, P.L. Stanghellini, The vibrational spectra of the cyanide ligand revisited: the v(CN) infrared and Raman spectroscopy of Prussian blue and its analogues, J. Raman Spectrosc. 42 (2011) 2006–2014. https://doi.org/10.1002/jrs.2944.

[44] A.N. Murashkevich, A.S. Lavitskaya, T.I. Barannikova, I.M. Zharskii, Infrared absorption spectra and structure of TiO2-SiO2 composites, J. Appl. Spectrosc. 75 (2008) 730–734. https://doi.org/10.1007/s10812-008-9097-3.

[45] P.J. Kulesza, M.A. Malik, A. Denca, J. Strojek, In Situ FT-IR/ATR Spectroelectrochemistry of Prussian Blue in the Solid State, Anal. Chem. 68 (1996) 2442–2446. https://doi.org/10.1021/ac950380k.

[46] L. Samain, F. Grandjean, G.J. Long, P. Martinetto, P. Bordet, D. Strivay, Relationship between the Synthesis of Prussian Blue Pigments, Their Color, Physical Properties, and Their Behavior in Paint Layers, J. Phys. Chem. C. 117 (2013) 9693–9712. https://doi.org/10.1021/jp3111327.

[47] S. Umapathy, A.J. McQuillan, R.E. Hester, An in situ resonance Raman and infrared spectroscopic study of hexacyanoferrate (II) ion adsorbed to aqueous colloidal TiO2, Chem. Phys. Lett. 170 (1990) 128–132. https://doi.org/https://doi.org/10.1016/0009-2614(90)87103-X.

[48] M. Thommes, K. Kaneko, A. V Neimark, J.P. Olivier, F. Rodriguez-Reinoso, J. Rouquerol, K.S.W. Sing, Physisorption of gases, with special reference to the evaluation of surface area and pore size distribution (IUPAC Technical Report), Pure Appl. Chem. 87 (2015) 1051–1069. https://doi.org/10.1515/pac-2014-1117.

[49] M. Valari, A. Antoniadis, D. Mantzavinos, I. Poulios, Photocatalytic reduction of Cr(VI) over titania suspensions, Catal. Today. 252 (2015) 190–194. https://doi.org/https://doi.org/10.1016/j.cattod.2014.10.014.

[50] S. Luo, Y. Xiao, L. Yang, C. Liu, F. Su, Y. Li, Q. Cai, G. Zeng, Simultaneous detoxification of hexavalent chromium and acid orange 7 by a novel Au/TiO2 heterojunction composite nanotube arrays, Sep. Purif. Technol. 79 (2011) 85–91. https://doi.org/https://doi.org/10.1016/j.seppur.2011.03.019.

[51] M.I. Litter, Mechanisms of removal of heavy metals and arsenic from water by TiO2-heterogeneous photocatalysis, Pure Appl. Chem. 87 (2015) 557. https://doi.org/10.1515/pac-2014-0710.

[52] S. Nappini, A. Matruglio, D. Naumenko, S. Dal Zilio, M. Lazzarino, F.M.F. De Groot, C. Kocabas, O. Balci, E. Magnano, Graphene Nanoreactors: Photoreduction of Prussian Blue in Aqueous Solution, J. Phys. Chem. C. 121 (2017) 22225–22233. https://doi.org/10.1021/acs.jpcc.7b07898.